https://doi.org/10.5194/egusphere-2026-2532
Preprint. Discussion started: 22 June 2026

A computationally efficient TVD-FFSL hybrid tracer transport scheme on spherical centroidal voronoi tessellations in iAMAS (v2.6.3)

Gudongze Li[1], Chun Zhao[1,2], Yinhua Xia[3], Li Dong[4], Yibo Xue[1], Xiao-Xiao Zhang[5], Jun Gu[6], Jiawang Feng[1], and Zihan Xia[1]

[1]School of Earth and Space Sciences/Joint Laboratory of Fengyun Remote Sensing/State Key Laboratory of Fire Science/Institute of Advanced Interdisciplinary Research on High-Performance Computing Systems and Software, University of Science and Technology of China, Hefei, China
[2]Laoshan Laboratory, Qingdao, China
[3]School of Mathematical Sciences, University of Science and Technology of China, Hefei, China
[4]Institute of Atmospheric Physics, Chinese Academy of Sciences, Beijing, China
[5]State Key Laboratory of Ecological Safety and Sustainable Development in Arid Lands, Xinjiang Institute of Ecology and Geography, Chinese Academy of Sciences, Urumqi, China
[6]Department of Atmospheric and Oceanic Sciences, Fudan University, Shanghai, China

Correspondence: Chun Zhao (chunzhao@ustc.edu.cn)

Abstract. Tracer transport is a critical computational bottleneck in high-resolution atmospheric chemistry models, where tens to hundreds of species are advected. The iAMAS model (v2.6.3) on spherical centroidal Voronoi tessellations (SCVTs) currently employs a scheme (2H1FCT) that performs two steps of third-order transport followed by one step of flux-corrected transport (FCT), in which the FCT correction step dominates computational cost. This study develops TVD-FFSL, a computationally efficient hybrid tracer transport scheme. Horizontally, a total variation diminishing (TVD) flux operator with the KOREN limiter is employed. Vertically, a flux-form semi-Lagrangian (FFSL) operator based on piecewise parabolic method reconstruction handles cells with CFL > 1 unconditionally. Together with a second-order TVD Runge-Kutta time integration, the scheme ensures monotonicity without a separate FCT step. Idealized 2D tests demonstrate that TVD-FFSL achieves robust shape preservation. Although its errors are slightly higher than 2H1FCT, superior convergence rates render the accuracy gap negligible at finer resolutions ($\Delta x \leq 30$km). Realistic 3D dust simulations on a 16–60 km variable-resolution grid confirm its long-term stability and accuracy comparable to 2H1FCT. Performance benchmarks show that TVD-FFSL achieves over $2\times$ speedup in standalone transport tests and exceeds $3.75\times$ speedup in long-term atmospheric dust simulations, significantly reducing the computational overhead of numerous tracer transport. The design principles of TVD-FFSL could be transferable to other unstructured meshes, offering a pathway toward accelerating high-resolution atmospheric chemistry simulations.

https://doi.org/10.5194/egusphere-2026-2532
Preprint. Discussion started: 22 June 2026

1 Introduction

Air pollution poses severe threats to human health and terrestrial ecosystems globally (Chen et al., 2024; Richard et al., 2024). Besides, atmospheric tracers including greenhouse gases and aerosols exert profound impacts on the earth energy budget and thus global climate (Li et al., 2022). In past decades, atmospheric chemistry models (ACMs) were developed to integrate nonlinear meteorological processes with complex chemical kinetics (Simpson et al., 2023). These advanced models are typically required to track dozens to hundreds of tracers to enable researchers to simulate severe air pollution episodes (Coen et al., 2013; Yoon et al., 2024), or to evaluate the weather and climate effects of atmospheric tracers. However, the simultaneous transport of numerous tracers imposes a substantial computational burden. This challenge is further amplified as the scientific community pushes models toward kilometer-scale resolutions. High-resolution simulations not only increase grid cell numbers in computational domains but also necessitate smaller time steps due to the Courant-Friedrichs-Lewy (CFL) condition. Advection for numerous tracers is solved at every dynamical step, while their radiative and chemical processes are computed at much lower frequencies. The tracer transport module therefore becomes a critical bottleneck limiting overall efficiency and broader application of high-resolution ACMs.

The iAMAS is a physics-chemistry coupled atmospheric model (Feng et al., 2023; Gu et al., 2022) built upon the MPAS-A dynamical core (Skamarock et al., 2012) on spherical centroidal Voronoi tessellations (SCVTs). The SCVT mesh allows for smooth resolution refinement over target regions. Supported by the Sunway supercomputer platform, iAMAS has achieved global 3 km (U3km) simulations with online-coupled aerosols (Gu et al., 2022). Performance profiling of the U3km experiment reveals that two modules associated with tracer transport account for approximately 56.1% of the total execution time (Gu et al., 2022, Fig. 3b), when simulating 104 tracers. This computational overhead underscores the urgent need for a more computationally efficient transport scheme within variable-resolution framework based on SCVT.

To understand this bottleneck, it is essential to first examine the formulation and algorithmic structure of the current transport scheme in iAMAS inherited from the MPAS-A, hereafter referred to as the 2H1FCT scheme. The theoretical origin of the 2H1FCT scheme can be traced back to classical Eulerian finite volume methods combined with Runge-Kutta time forward schemes adopted in WRF model (Wicker and Skamarock, 2002; Skamarock et al., 2019). High-order flux operators in Wicker and Skamarock (2002) are constructed through taylor series expansions, which can not be directly used on unstructured meshes like SCVT. Skamarock and Gassmann (2011) developed new third- and fourth-order flux operators for SCVTs based on least-squares polynomial reconstruction. This approach uses second-order polynomials to estimate second-order directional derivatives in high-order flux formulas originating from Wicker and Skamarock (2002). To achieve better numerical stability and allow for larger time steps, the time-splitting scheme employed in iAMAS is the variant of the third-order Runge-Kutta method in Wicker and Skamarock (2002) with modified sub-steps $\Delta t/2$, $\Delta t/2$, and Δt, maintaining effective second-order accuracy. For nonlinear transport, the original third-order Runge-Kutta scheme degenerates to second-order accuracy (Klemp et al., 2007), so this variant incurs no accuracy loss in real atmospheric simulations. However, such scheme still can not guarantee monotonicity, which is crucial for tracer transport to prevent spurious oscillations and unphysical values. Following the strategy adopted in WRF (Wang et al., 2009), the third step of Runge-Kutta integration incorporates the flux-corrected trans-

https://doi.org/10.5194/egusphere-2026-2532
Preprint. Discussion started: 22 June 2026

port (FCT) method (Zalesak, 1979; Skamarock, 2006), which dynamically corrects fluxes using coefficients derived from the monotonicity constraints. The current 2H1FCT scheme thus comprises two third-order transport steps and one FCT correction step per dynamical time step, where the FCT step blends the third-order and first-order upwind fluxes. While the 2H1FCT scheme is numerically robust and monotonic, its multi-step structure makes it computationally demanding, especially for numerous tracers. With precomputed coefficients, the third-order transport step can achieve high computational efficiency, but the FCT step requires approximately 4 times the computational cost of the third-order step. Besides flux correction associated with calculation of both third-order and first-order fluxes, the FCT limiter also necessitates neighborhood searches to identify local extrema and additional communications to exchange flux correction coefficients of all tracers. Consequently, the 2H1FCT becomes the most expensive module in the iAMAS model, when scaled up to hundreds of tracers at kilometer-scale resolutions.

Over the past decades, various algorithms have been implement in atmospheric tracer transport, generally categorized into Lagrangian, semi-Lagrangian methods and Eulerian methods. ATTILA (Reithmeier and Sausen, 2002), CLaMS (McKenna et al., 2002) and FLEXPART (Stohl et al., 2005) are examples of chemical transport schemes based on Lagrangian parcel tracking, which are discretized by tracer parcels. Compared to Eulerian methods, Lagrangian methods are less susceptible to numerical diffusion and unconditionally stable to allow for larger time steps. These advantages have motivated efforts to integrate Lagrangian transport schemes into grid-based atmospheric models. ECHAM4 using ATTILA to transport water vapor and cloud water had more realistic water vapor distribution over extratropics at stratosphere (Stenke and Grewe, 2005) than results in simulations with semi-Lagrangian methods. CLaMS was online coupled with ECHAM/MESSy Atmospheric Chemistry (EMAC) model to transport chemical species, improving transport of chemical species, especially at the edge of the polar vortex compared with the original scheme (Hoppe et al., 2014). However, coupling Lagrangian schemes into fixed-grid models poses inherent challenges in parallel implementation (Dong et al., 2014), which become especially pronounced in high-resolution simulations requiring massive parallelism. Moreover, to mitigate the parcel disorder problem under severely deforming flows, additional techniques such as periodic remeshing (Bosler et al., 2017) are often necessary, potentially offsetting the efficiency advantage gained from larger time steps.

Semi-Lagrangian methods offer a practical compromise, retaining the stability advantage of large time steps from the Lagrangian framework while operating naturally on Eulerian grids. Conventional semi-Lagrangian methods typically involve two steps: backward trajectory tracking and interpolation from the Eulerian grid to the departure point. However, the interpolation step may introduce conservation errors. Therefore, Iske and Käser (2004) proposed a conservative scheme on Voronoi diagrams using piecewise linear polynomials, which is of particular relevance to SCVT-based meshes. Lauritzen et al. (2010) extended the conservative remapping approach of Dukowicz and Kodis (1987) to cubed-sphere grids, developing the conservative semi-Lagrangian multi-tracer transport scheme (CSLAM). An alternative approach is the flux-form semi-Lagrangian (FFSL) scheme, which naturally ensures conservation by integrating fluxes across cell interfaces within a finite volume framework (Lin and Rood, 1996). Therefore, a flux-form version of CSLAM (FF-CSLAM) was developed by Harris et al. (2011) for cubed-sphere grids, which retains the shape-preserving properties of CSLAM and enables the flux-limited monotonicity to reduce diffusion. Lauritzen et al. (2011) further simplified the FF-CSLAM scheme using the swept area approach (Hirt et al., 1974), making the implementation simpler and more robust. For CFL $\leq 1/2$, the simplified scheme even achieves higher

https://doi.org/10.5194/egusphere-2026-2532
Preprint. Discussion started: 22 June 2026

accuracy than the original scheme. Dubey et al. (2014) implemented the FF-CSLAM scheme for icosahedral-hexagonal grids using a weighted least squares method for bi-quadratic polynomial reconstruction. They assessed different flux-area approximations and found that reducing derivative errors through higher-order reconstructions has a more significant impact on overall accuracy than minimizing geometrical errors in simplified flux-area calculations.

The computational advantage of semi-Lagrangian methods lies in their unconditional stability, which allows larger time steps. Although backward trajectory is independent of tracer species, the cost of interpolation and monotonicity limiting for each tracer remains non-negligible, potentially even exceeding that of the third-order transport step in the 2H1FCT scheme. If the time step is constrained by the computational stencil or by other model components (as in iAMAS), the efficiency gain for multi-species transport becomes limited. Moreover, Dubey et al. (2014) showed that FF-CSLAM still requires an FCT procedure for satisfactory monotonicity, further diminishing its efficiency advantage.

Consequently, total variation diminishing (TVD) schemes, which guarantee monotonicity by design, emerge as a compelling alternative for efficient transport. However, high-order TVD schemes developed in one dimension cannot be directly applied to two-dimensional unstructured meshes (Bruner et al., 1997), prompting the development of various extension strategies. One class of methods constructs the flux at each cell interface using three nodes: the downwind cell D, the upwind cell C, and a further upwind cell U (Bruner et al., 1997; Darwish and Moukalled, 2003; Li et al., 2008; Hou et al., 2011, 2012). The geometric complexity of 2D unstructured meshes makes cell U unable to be identified directly. Bruner et al. (1997) estimated the value at cell U through extrapolation from cell C and its first-order neighbors. Darwish and Moukalled (2003) later proposed a gradient-based extrapolation at cell C to reconstruct the value at cell U, which better preserves the TVD property than the approach of Bruner et al. (1997). Li et al. (2008) took a different approach by identifying the cell U_r which is closest to the virtual cell U based on the geometric relation between cells C and D, then interpolating within cell U_r to estimate the value at U, achieving even better convergence rates than the Darwish and Moukalled (2003) scheme. Hou et al. (2012) adopted a similar strategy to Li et al. (2008) and further incorporated the mesh geometry into calculation of flux limiters.

The present study aims to develop a computationally efficient transport scheme while maintaining stability and monotonicity. A TVD scheme incurs only the modest overhead of flux limiter evaluations beyond a standard finite volume method, while its built-in monotonicity eliminates the need for a separate FCT step. Although Li et al. (2008) yields better convergence, the cell U_r may require an additional halo layer when encountering pentagonal cells in SCVT meshes (cell 5 in Fig. 1). Therefore, the horizontal direction adopts a TVD scheme with the Darwish and Moukalled (2003) reconstruction. Since iAMAS occasionally has CFL > 1 cells at vertical direction, an FFSL scheme is adopted for its unconditional stability and finite volume compatibility. Time integration uses a TVD Runge-Kutta method to suppress spurious oscillations in conjunction with the TVD flux operator.

This paper is organized as follows: Section 2 describes the iAMAS model and TVD-FFSL hybrid scheme. Section 3 evaluates the TVD-FFSL scheme through two-dimensional test cases, comparing it with the original 2H1FCT scheme. Section 4 assesses TVD-FFSL scheme in realistic three-dimensional atmospheric simulations with dust aerosols. Section 5 compares the computational efficiency and scalability of TVD-FFSL scheme with the 2H1FCT scheme. Finally, Section 6 presents the conclusions and discussions.

https://doi.org/10.5194/egusphere-2026-2532
Preprint. Discussion started: 22 June 2026

2 Method

2.1 iAMAS v2.6.3

iAMAS is a high-performance, highly scalable physics-chemistry coupled atmospheric model built upon the MPAS-A dynamical core (Skamarock et al., 2012), specifically optimized for the Sunway heterogeneous supercomputing platform. Feng et al. (2023) first incorporated natural-source aerosols such as dust and sea salt into the variable-resolution framework based on SCVT meshes, together with their associated processes including dry and wet deposition, aerosol–radiation interactions, and aerosol–cloud interactions. Gu et al. (2022) adapted iAMAS to the Sunway heterogeneous architecture with optimizations including vectorization and parallel fragmented I/O. Xia et al. (in preparation) further integrated anthropogenic emissions and gas-phase chemical mechanisms such as SAPRC99, advancing the model to iAMAS v2.6. The TVD-FFSL scheme proposed by this work is implemented in iAMAS v2.6.3. Currently, iAMAS has been applied to typhoon prediction (Gu et al., 2025), monsoon subseasonal prediction (Gu et al., 2024; Li et al., 2025), polar meteorology (Yang et al., 2025), and dust climate effects (Feng et al., 2025).

2.2 TVD-FFSL hybrid scheme

The tracer transport equation describes the conservation of tracer mass. In the transport scheme, only the advective transport term is considered, while source and sink terms as well as diffusion are excluded from the formulation. To ensure mass conservation, the equation is cast in flux form as follows (Skamarock and Menchaca, 2010; Dubey et al., 2014):

$$\frac{\partial(\rho\psi)}{\partial t} = -\nabla\cdot(\mathbf{V}\rho\psi) \tag{1}$$

where ρ is the density of dry air, ψ is the mixing ratio of tracer, $\mathbf{V}$ is the velocity vector. Applying the finite volume method, Eq. 1 is integrated over each grid cell and the divergence theorem transforms the volume integral into a surface flux integral, resulting in the following discrete form:

$$\frac{\partial\rho\bar{\psi}_{ik}}{\partial t} = -\frac{1}{A_i}\sum_{j=1}^{N_i} d_{ij}F^h_{ikj}\left(\mathbf{V^h},\rho,\psi\right) - \frac{1}{H_k}\sum_{m=1}^{2} F^v_{ikm}\left(w,\rho,\psi\right) \tag{2}$$

where i denotes the horizontal grid cell index, k denotes the vertical level index, $\rho\bar{\psi}_{ik}$ represents the cell-averaged tracer mass, A_i is the horizontal area, N_i is the number of neighboring cells of cell i, d_{ij} is the length of the edge shared by cells i and its j-th neighbor, F^h_{ikj} denotes the horizontal flux, $\mathbf{V}^h$ is the horizontal velocity vector, H_k is the thickness of vertical layer k, F^v_{ikm} represents the vertical flux, and w is the vertical velocity.

Given that the atmosphere behaves as a thin fluid layer with vastly different horizontal and vertical scales, atmospheric solvers typically employ distinct coordinate systems for horizontal and vertical directions. In iAMAS, the horizontal coordinate surface is discretized using SCVT, whereas the vertical coordinate adopts a hybrid terrain-following ζ coordinate proposed by Klemp (2011). Consequently, horizontal and vertical fluxes in Eq. 2 are computed separately, despite sharing the same algorithmic framework in the 2H1FCT scheme (Skamarock and Gassmann, 2011). There is a rule of thumb about relation

https://doi.org/10.5194/egusphere-2026-2532
Preprint. Discussion started: 22 June 2026

between maximum time step Δt_{max} (s) and minimum grid spacing Δx_{min} (km) for iAMAS (Wicker and Skamarock, 2002; Skamarock et al., 2019):

$$\Delta t_{max} \approx 6\Delta x_{min} \tag{3}$$

The maximum time step given by Eq. 3 ensures CFL ≤ 1 for horizontal advection except under extreme wind speeds exceeding approximately 166 m/s. Consequently, TVD-type algorithms can be applied horizontally without additional time step restriction. In contrast, vertical advection may result in CFL > 1 for few grid cells. For instance, in real atmospheric simulations with the U60km mesh, approximately 0.015% of cells exhibit CFL > 1. Although these cells with unstable conditions constitute a negligible fraction of the total, they can still trigger instability in vertical advection, which then compromises the entire transport computation. Therefore, unconditionally stable methods such as the FFSL scheme are well-suited for formulating the vertical flux operator.

The TVD-FFSL hybrid scheme proposed in this study integrates TVD and FFSL methods for atmospheric transport on SCVTs. Horizontally, the scheme employs Darwish TVD scheme with KOREN flux limiters to ensure monotonicity and second-order accuracy, while avoiding FCT frameworks to improve computational efficiency. Vertically, the FFSL method based on piecewise parabolic method (PPM) reconstruction provides unconditional stability and guarantees monotonicity without flux correction. Time integration uses the optimal second-order TVD Runge-Kutta method (Shu and Osher, 1988; Gottlieb and Shu, 1998), achieving efficient and stable solutions. The individual components are detailed in the following subsections.

2.2.1 Horizontal flux operator

iAMAS employs C-Grid staggering to distribute variables on SCVTs horizontally, with air density ρ and tracer mixing ratio ψ defined at cell centers (black dot in Fig. 1), while the velocity components $\mathbf{V}^h$ are defined at cell faces (red vector in Fig. 1). Since ρ and $\mathbf{V}^h$ are determined by the other governing equations, they can be treated as known quantities within the transport scheme. Consequently, the horizontal flux in Eq. 2 is computed as:

$$F_{ij}^h = \rho_{ij}\mathbf{V}_{ij}^h\psi_{ij} \tag{4}$$

where subscript ij denotes the shared edge between cell i and its j-th neighbor. Since the horizontal flux calculation is identical at all vertical levels, the subscript k is omitted for brevity. The critical step is estimating the tracer concentration at cell edges, ψ_{ij}, based on cell-centered values. When velocity flows from cell i to its j-th neighbor, cell i corresponds to Cell C and the neighbor corresponds to Cell D. The notation reverses when velocity flows in the opposite direction. Then, $\psi_{(C,D)}$ of a TVD scheme with flux limiter on unstructured grids is written as (Bruner et al., 1997; Darwish and Moukalled, 2003):

$$\psi_{(C,D)} = \psi_C + \frac{1}{2}\phi(r_{(C,D)})(\psi_D - \psi_C) \tag{5}$$

where $r_{(C,D)}$ is the upwind ratio of consecutive gradients, whose exact definition is:

$$r_{(C,D)} = \frac{\psi_C - \psi_U}{\psi_D - \psi_C} \tag{6}$$

https://doi.org/10.5194/egusphere-2026-2532
Preprint. Discussion started: 22 June 2026

And $\phi(r_{(C,D)})$ is the flux limiter, used to suppress spurious oscillations near discontinuities while maintaining high-order accuracy in smooth regions. However, the virtual cell U which is the upstream cell of Cell C can not be determined concisely on unstructured grids. Here, Darwish extraplolation method (Darwish and Moukalled, 2003) is employed, whose $r_{(C,D)}$ is defined as:

$$r_{(C,D)} = \frac{2\nabla\psi_C \cdot \boldsymbol{d_{CD}}}{\psi_D - \psi_C} - 1 \tag{7}$$

where $\boldsymbol{d_{CD}}$ denotes the vector from the center of cell C to the center of cell D, and $\nabla\psi_C$ represents the tracer concentration gradient at the center of cell C. The gradient is estimated using second-order polynomial reconstruction following Skamarock and Gassmann (2011). While the original formulation employs the polynomial to estimate second-order directional derivatives for high-order flux operators, we adopt the same reconstruction to compute the first-order gradient required by the Darwish TVD scheme. Detailed description are provided in Appendix A.

The limiter function $\phi(r_{(C,D)})$ (Sweby, 1984) adaptively controls the reconstruction of $\psi_{(C,D)}$ based on the smoothness indicator $r_{(C,D)}$, suppressing oscillations near discontinuities while preserving accuracy in smooth regions. For one-dimensional uniform grids, the MINMOD and SUPERBEE limiters bound the second-order TVD region (Sweby, 1984; Tang, 2023). Limiter functions within this region (Fig. 2) maintain monotonicity while preserving second-order accuracy (Sweby, 1984). While the theoretical framework above applies to one-dimensional uniform grids, verification through testing is required for two-dimensional SCVT meshes. Numerical experiments reveal that limiters closer to MINMOD exhibit greater numerical dissipation, whereas those approaching SUPERBEE show reduced dissipation but compromised shape-preserving properties. Based on extensive testing and quantitative evaluation, we selected the KOREN limiter (Koren, 1993):

$$\phi(r) = \begin{cases} \min\left(2r, \frac{2+r}{3}, 2\right), & \text{if } r > 0 \\ 0, & \text{if } r \leq 0 \end{cases} \tag{8}$$

The KOREN limiter achieves third-order accuracy in smooth regions ($r_{(C,D)} \approx 1$) while maintaining robust monotonicity preservation near discontinuities. Compared to other TVD limiters, KOREN offers an optimal balance between numerical dissipation and oscillation suppression when applied to atmospheric transport problems (see Sec. 3). Geometry-dependent limiters proposed in Hou et al. (2011, 2012) show promise for specific applications. However, for atmospheric transport simulations on SCVT meshes, we find that conventional limiters unexpectedly offer better performance.

The horizontal flux operator in the TVD-FFSL scheme employs the Darwish TVD construction adapted for SCVT meshes. Since the flux at each edge depends on tracer concentrations at the upwind cell and its first-order neighbors, the horizontal flux operator requires a halo depth of two (i.e., two layers of halo cells). This matches the communication depth of the original 2H1FCT scheme in iAMAS, resulting in equivalent data volume per communication. The computation of factor $r_{(C,D)}$ reduces to a dot product of precomputed weights and tracer concentrations at the upwind cell and its neighbors, followed by direct flux calculation through Eqs. 5 and 4. While the computational cost is slightly higher than the third-order flux operator in 2H1FCT, this approach is more efficient than the flux correction procedure and eliminates one communication step for flux correction coefficients of all tracers. Consequently, the horizontal flux operator achieves theoretical monotonicity and second-order accuracy with improved computational efficiency. The practical performance of this scheme is evaluated in Sec. 3.

https://doi.org/10.5194/egusphere-2026-2532
Preprint. Discussion started: 22 June 2026

2.2.2 Vertical flux operator

In the vertical direction, the flux construction reduces to a one-dimensional transport problem on non-uniform grids, which is considerably simpler than the horizontal SCVT framework. However, vertical advection presents challenges with CFL > 1 at few grids. Resolving these time step restrictions through substepping would impose a significant computational burden, particularly for simulations with numerous cells and multiple tracer species. Consequently, then FFSL scheme emerges as the optimal choice due to its unconditional stability, strong conservation properties, and excellent scalability with respect to the number of tracer species under identical wind field configurations.

A critical component of the FFSL scheme is trajectory calculation, which determines the departure point z_{dep} through backward tracking. Specifically, z_{dep} is the location from which a tracer parcel originates and reaches the target interface z_{int} after traveling against the wind for one time step Δt. Rather than employing high-order substepping methods (Giraldo, 1999; Rosatti et al., 2005; Ullrich et al., 2012) that require multiple substeps and wind field interpolation, we adopt a direct first-order approximation:

$$z_{\text{dep}} = z_{\text{int}} - \Delta t\, w(z_{\text{int}}) \tag{9}$$

Despite its simplicity, this approach demonstrates both computational efficiency and good practical performance in atmospheric transport simulations. We attribute this to three primary factors: (1) the vertical velocity used is the average of values before and after Runge-Kutta integration in the iAMAS, (2) geometrical errors from simplified trajectory calculations have less impact on overall accuracy than the quality of polynomial reconstruction (Dubey et al., 2014), and (3) grid cells with CFL > 1 constitute a negligible fraction of the total.

With the departure point determined, the vertical flux is computed as follows:

$$F_k^v = \int_{z_{\text{dep}}}^{z_{\text{int}}} \rho\psi dz \tag{10}$$

Following the FFSL formulation (Lin and Rood, 1996), the tracer distribution is reconstructed using the PPM (Colella and Woodward, 1984), which provides third-order accuracy and good monotonicity preservation. This approach is particularly well-suited for resolving smooth and stratified vertical profiles of atmospheric tracers such as dust and sea salt. Details of PPM are provided in Appendix B.

To ensure high computational efficiency, the PPM reconstruction are highly vectorized in this TVD-FFSL implementation. The traditional PPM schemes suffer from conditional branching associated with the monotonicity limiters (Eq. B2). Explicit if-then-else statements inside loops typically inhibit Single Instruction Multiple Data (SIMD) vectorization and cause performance penalties due to branch misprediction (Chopp, 2019). To overcome this, the PPM reconstruction is implemented in an array-oriented, branch-free programming paradigm, as outlined in Algorithm 1. Instead of evaluating conditions sequentially for each vertical layer, the limiter constraints are evaluated simultaneously across the entire vertical column to generate boolean masks $\mathbf{M_1}$, $\mathbf{M_2}$ and $\mathbf{M_3}$. Using intrinsic masked assignments (the MERGE operation), the modified interface values ψ_B, ψ_U (Eq. B2) and the subsequent polynomial coefficients $\boldsymbol{C}_0$, $\boldsymbol{C}_1$, $\boldsymbol{C}_2$ (Eq. B7) are computed through continuous array operations.

https://doi.org/10.5194/egusphere-2026-2532
Preprint. Discussion started: 22 June 2026

Combined with the intrinsic advantage of the FFSL scheme, this vectorized calculation of scalar coefficients minimizes the marginal computational cost of adding tracers.

2.2.3 TVD Runge-Kutta method

When the spatial discretization scheme follows the TVD framework, TVD Runge-Kutta timestepping methods provide excellent compatibility and effectively avoid the oscillations that can arise from non-TVD Runge-Kutta schemes (Gottlieb and Shu, 1998). The TVD time integration preserves the monotonicity maintained by the horizontal discretization, ensuring as much as possible that the hybrid scheme remains TVD in both space and time. The optimal second-order TVD Runge-Kutta method (Shu and Osher, 1988; Gottlieb and Shu, 1998) is selected in this transport scheme, shown below:

$$\begin{aligned}\rho\bar{\psi}^{(1)} &= \rho\bar{\psi}^{n} + \Delta t \mathrm{L}(\rho\bar{\psi}^{n}) \\ \rho\bar{\psi}^{n+1} &= \frac{1}{2}\rho\bar{\psi}^{n} + \frac{1}{2}\rho\bar{\psi}^{(1)} + \frac{1}{2}\Delta t L(\rho\bar{\psi}^{(1)})\end{aligned} \tag{11}$$

where L denotes the spatial operator. The third-order TVD Runge-Kutta scheme (Gottlieb and Shu, 1998) was also tested but yielded degraded accuracy, possibly because the spatial flux operator is also second-order. Through testing, the second-order scheme demonstrated better performance with higher computational efficiency.

3 2D test results

Following previous studies (Skamarock and Menchaca, 2010; Skamarock and Gassmann, 2011; Dong et al., 2014), two idealized 2D test cases are examined: solid body rotation and deformational flow. Since these tests evaluate only horizontal transport, they validate the horizontal TVD method of the proposed TVD-FFSL scheme compared with the 2H1FCT scheme.

3.1 Solid body rotation

The solid body rotation test is a standard benchmark for transport schemes, characterized by a non-divergent velocity field that completes one full rotation per period T. As a basic test without deformational flow, it evaluates the spatial accuracy, numerical dissipation, and shape-preserving capabilities of transport schemes. Following Skamarock and Menchaca (2010), we employ the Earth sphere as the test domain to better approximate atmospheric transport conditions, rather than the conventional unit sphere. The zonal velocity is set as:

$$u = \cos(\lambda)\frac{2\pi R_e}{T} \tag{12}$$

where R_e is the Earth's radius and λ denotes latitude. The meridional velocity component is set to zero. Under this velocity field, the tracer distribution returns to its initial state after one period T.

We test two initial conditions under the solid body rotation case: a cosine bell (Williamson et al., 1992) and a slotted cylinder (Lipscomb and Ringler, 2005), shown in Fig. 3a and Fig. 5a, respectively. All parameter configurations are identical to those in Skamarock and Menchaca (2010). Table 1 lists the meshes used in these tests. It should be noted that all SCVT meshes used in

https://doi.org/10.5194/egusphere-2026-2532
Preprint. Discussion started: 22 June 2026

this study are generated by the Jigsaw algorithm (Engwirda, 2017), which differs from the traditional Lloyd algorithm (Renka, 1997) used for SCVT mesh generation. Consequently, the 2H1FCT test results in this paper may show slight discrepancies from those reported in Skamarock and Gassmann (2011) due to mesh differences.

3.1.1 Cosine bell

Fig. 3 displays the spatial distributions of the cosine bell after one full revolution. Visually, both the 2H1FCT and TVD-FFSL schemes accurately transport the tracer without noticeable phase errors or structural distortions. The concentric contours remain highly symmetric, demonstrating that the TVD-FFSL scheme possesses excellent shape-preserving characteristics. A closer examination of the global extrema reveals that both schemes perfectly maintain the strict positivity of the tracer field, without negative values. The maximum peak value of the TVD-FFSL scheme (976.09) is slightly lower than that of the 2H1FCT scheme (989.54). This minor peak clipping may be due to the flux limiters used in the TVD scheme, which introduce moderate numerical dissipation near local extrema to suppress spurious oscillations.

The L_2 and L_{inf} error norms (Appendix C) are chosen to quantitatively evaluate the spatial accuracy of the transport schemes (Dubey et al., 2014; Dong et al., 2014). Both schemes exhibit a systematic reduction in errors as the resolution increases (Fig. 4). Notably, while the L_{inf} error (red dash line) of the TVD-FFSL scheme is higher due to the aforementioned TVD limiter effect at the peak, its L_2 error (red solid line) is highly competitive. At coarser resolutions, the L_2 error of TVD-FFSL is comparable to 2H1FCT, and at higher resolutions (number of cells $> 10^5$, $\Delta x = 60$km), TVD-FFSL even slightly outperforms the original scheme, showing lower overall numerical dissipation across the global domain.

Although both schemes achieve near second-order convergence, the convergence rates exhibit variations across different resolutions (Fig. 4). Table 2 further details the L_2 and L_{inf} convergence rates. The TVD-FFSL scheme demonstrates superior convergence behavior at coarse resolutions. For the transition from 240km to 120km, TVD-FFSL achieves a remarkable super-convergence rate of 2.457, compared to 1.663 for 2H1FCT. From 120km to 60km, it maintains a robust rate of 1.809, closely approaching the theoretical second-order limit. At the finest resolution step (60km–30km), the convergence rates for both schemes drop to approximately 1.39. Overall, the convergence behavior of TVD-FFSL is comparable to, and to some extent superior to, that of 2H1FCT.

3.1.2 Slotted Cylinder

In contrast to the smooth cosine bell, the slotted cylinder presents a more rigorous test with sharp discontinuities (Fig. 5a) that challenge shape-preserving capabilities and oscillation suppression of transport schemes.

Fig. 5b and Fig. 5c show the slotted cylinder distributions after one revolution, simulated by the 2H1FCT and TVD-FFSL schemes, respectively. Both schemes exhibit a certain degree of inherent numerical diffusion, resulting in the smoothing of the originally sharp edges. However, the overall cylinder structure is well maintained by both schemes, and the central "slot" remains distinct and clearly resolved. Crucially, the TVD-FFSL scheme effectively controls numerical oscillations and maintains strict positivity without requiring flux correction, preventing any non-physical negative values. Regarding peak values,

https://doi.org/10.5194/egusphere-2026-2532
Preprint. Discussion started: 22 June 2026

both schemes show slight overshoots above 1000.0. TVD-FFSL demonstrates marginally better overshoot control (1012.21) compared to 2H1FCT (1013.56).

The error norms for the slotted cylinder test are shown in Fig. 6. With discontinuous initial conditions, error characteristics differ markedly from smooth fields. The L_{inf} errors remain resolution-independent, as expected for transport of discontinuous fields. Numerical diffusion inherently smears sharp edges, causing errors that persist regardless of grid spacing. TVD-FFSL demonstrates marginally higher L_2 errors than 2H1FCT, though the difference remains small. The slotted cylinder test thus confirms TVD-FFSL's robustness and shape preservation, performing comparably to 2H1FCT despite severe discontinuities.

3.2 2D deformational flow

While the solid body rotation test assesses basic advection without flow distortion, the 2D deformational flow test is a significantly more rigorous case. It features severe stretching and shearing, rolling the initial tracer field into filaments before reversing the flow to recover the initial field (Blossey and Durran, 2008). Skamarock and Menchaca (2010) designed a 2D deformational flow field test for Earth atmospheric transport scenarios, with the stream function given by (with minor corrections to typographical errors in the original formula):

$$\Psi(\bar{r},t) = \frac{4\pi R_e^2}{T}\Bigg\{\sin\lambda \pm \cos\Big(\frac{2\pi t}{T}\Big)\times \Big[\frac{\bar{r}^2}{2} + \frac{1}{96}\log(1-16\bar{r}^2+256\bar{r}^4) - \frac{1}{48}\log(1+16\bar{r}^2) - \frac{\sqrt{3}}{48}\arctan\Big(\frac{32\bar{r}^2-1}{\sqrt{3}}\Big)\Big]\Bigg\} \tag{13}$$

where $\bar{r} = \frac{\pi/2-\lambda}{\pi}$. The normal velocity at edge i_e is computed as:

$$V_{n,i_e} = \frac{\Psi_{v_{2,i_e}} - \Psi_{v_{1,i_e}}}{L_{i_e}} \tag{14}$$

where v_{1,i_e} and v_{2,i_e} are two vertices of edge i_e and L_{i_e} is the length of edge i_e.

We also test the smooth cosine bell initial condition under this scenario. Fig. 7 illustrates the time evolution of the cosine bell at $t = \frac{T}{4}, \frac{T}{2}, \frac{3T}{4}$ and $t = T$ for both the 2H1FCT and TVD-FFSL schemes. Visually, both schemes perform excellently. At $t = \frac{T}{4}$ and $t = \frac{3T}{4}$, the initial bell is intensely stretched. The TVD-FFSL scheme smoothly captures this filamentary structure without breaking it up into unphysical discrete blobs, demonstrating robust shape-preserving capabilities under strong deformation. Upon the flow reversal at $t = \frac{T}{2}$ and $t = T$, both schemes successfully reconstruct the original bell shape. Consistent with the findings in the solid body rotation test, maximum values at $t = T$ reveals that the TVD-FFSL scheme exhibits slightly more peak clipping (979.65) compared to the 2H1FCT scheme (988.10). TVD limiters naturally become more restrictive in strong deformation to prevent oscillations, which is an expected trade-off for stability.

Fig. 8 further illustrates the error norms of the cosine bell under deformational flow. The absolute values of both L_2 and L_{inf} error norms for the TVD-FFSL scheme are slightly larger than those of the 2H1FCT scheme across scales (from 240 km to 30 km). However, at the finest resolution (U30km, 658 591 cells), the difference in L_2 errors between TVD-FFSL and

https://doi.org/10.5194/egusphere-2026-2532
Preprint. Discussion started: 22 June 2026

2H1FCT becomes negligible. While absolute error magnitude is important, the convergence rate under grid refinement is of equal significance. As clearly demonstrated by the steeper slopes of the TVD-FFSL lines in Fig. 8 and detailed in Table 2, the TVD-FFSL scheme exhibits significantly superior convergence properties. When comparing errors between the 240km and 120km meshes, TVD-FFSL achieves a convergence rate of 2.394, higher than 2H1FCT (1.976). More importantly, between the 120km and 60km meshes, TVD-FFSL maintains a robust rate of 2.147, whereas the 2H1FCT scheme's rate degrades to 1.490. Even for the 60km–30km comparison, TVD-FFSL sustains a higher rate of 1.728 compared to 1.441 for 2H1FCT. In summary, despite slightly higher absolute errors, TVD-FFSL demonstrates superior convergence rates and successfully reconstructs strongly deformed tracer fields.

3.3 Summary of 2D tests

The 2D idealized tests validate the performance of the horizontal TVD component of the proposed TVD-FFSL hybrid scheme. Under solid body rotation, the scheme demonstrates excellent shape preservation for both smooth and discontinuous initial conditions, with minor peak clipping representing an acceptable trade-off for monotonicity. In deformational flow case, the horizontal TVD operator exhibits superior convergence properties compared to 2H1FCT, maintaining robust convergence rates across different mesh comparisons while successfully reconstructing strongly deformed tracer fields. These results confirm that the horizontal TVD component meets the requirements for accurate and reliable atmospheric transport.

4 Real test results

While the preceding idealized tests validate the mathematical properties of the horizontal TVD component, they do not examine the vertical FFSL operator nor guarantee reliability in realistic three-dimensional atmospheric simulations. To bridge this gap, the scheme has been fully coupled into iAMAS to simulate the transport of aerosol and chemical species such as dust, sea salt and NO_x. Such online coupling demands thorough validation of long-term numerical stability, robustness, and compatibility with other model components.

Thus, two dust-related experiments are conducted on a variable-resolution grid with regional refinement to 16 km (Fig. 9). The first experiment (hereafter Dust21) covers a 20-day period from 00:00 UTC on 12 March to 24:00 UTC on 31 March, 2021, which is characterized by frequent dust activity. This simulation is designed to assess the stability of TVD-FFSL and compare its behavior with 2H1FCT, using 512 CPU cores. The second experiment (hereafter Dust25) targets a severe dust storm event on November 26–27, 2025, featuring rapid transport processes. Dust25 was simulated from 00:00 UTC on 22 November to 00:00 UTC on 28 November, 2025, using 256 CPU cores. All simulations share identical configurations except for the transport schemes.

Fig. 10 presents the PM_{10} column concentration averaged over the 20-day Dust21 simulation period. The column-integrated quantity is chosen here as it reflects the accumulated effects of both horizontal and vertical transport. The spatial distributions produced by 2H1FCT (Fig. 10a) and TVD-FFSL (Fig. 10b) are in close agreement, both capturing the large-scale dust plumes over northern China and Mongolia. A quantitative comparison within the refined region (Fig. 10c) further confirms the con-

https://doi.org/10.5194/egusphere-2026-2532
Preprint. Discussion started: 22 June 2026

sistency between the two schemes, yielding an MAE of $0.117\,\mathrm{g\,m^{-2}}$ and a correlation coefficient of $\rho = 0.987$. Although the preceding idealized tests indicate that TVD-FFSL suppresses extrema more strongly than 2H1FCT, Fig. 10c reveals that TVD-FFSL yields slightly higher values than 2H1FCT in the high-concentration range. These results demonstrate that TVD-FFSL maintains numerical stability throughout the 20-day continuous simulation, with no evidence of unphysical drifts or spurious mass accumulation when coupled online in iAMAS.

The Dust25 experiment targets a severe dust storm that transported dust from northwestern to eastern China within two days, testing the TVD-FFSL robustness under extreme dust storm case. As the most direct indicator of rapid dust transport, we evaluate the simulated surface PM_{10} concentrations. Fig. 11 compares the daily averaged surface PM_{10} concentrationsagainst ground-based station observations from the China National Environmental Monitoring Centre (CNEMC) on November 26 and 27, 2025. Both schemes capture the southeastward propagation of the dust plume, with TVD-FFSL yielding moderately lower MAE and higher correlation coefficient over 2H1FCT on both days. However, since surface concentrations in ACMs are influenced by multiple processes such as emissions, boundary-layer mixing, these differences should be interpreted with caution. Rather than claiming superiority, the results demonstrate the robustness of TVD-FFSL under rapid transport conditions, achieving performance fully competitive with the 2H1FCT scheme in realistic applications.

5 Efficiency and scalability

As emphasized in the introduction, the computational efficiency of transport scheme is a critical bottleneck in high-resolution ACMs involving hundreds of tracer species. The primary objective of developing the TVD-FFSL scheme is to alleviate this computational burden while maintaining the accuracy and shape-preserving properties demonstrated in the previous sections.

Furthermore, state-of-the-art numerical weather prediction and climate models invariably rely on distributed-memory parallel computing environments. Therefore, evaluating the efficiency of a new algorithm must be conducted within a parallel framework. In this section, a series of performance tests are conducted on a high-performance computing cluster equipped with Intel Xeon E5-2680 v4 processors (2.40 GHz). We comprehensively assess the acceleration capability of the TVD-FFSL scheme relative to the original 2H1FCT scheme and compare their scalability regarding both the number of advected species and CPU cores.

First, the computational cost is evaluated as a function of the number of advected species, ranging from 8 to 200. This test is conducted on a U60km resolution grid utilizing a fixed computational resource of 8 nodes ($8 \times 28 = 224$ cores). The 2H1FCT scheme employs a second-order Runge-Kutta method with flux correction, performing three integrations per dynamical timestep. The first two are third-order transport calculations and the final step applies flux correction. The reported time cost per dynamical timestep represents the sum of these three components. In contrast, the TVD-FFSL scheme adopts the second-order TVD Runge-Kutta method, executing two transport calculations per dynamical timestep, with the total cost computed as the sum of both operations. Fig. 12 illustrates the wall-clock time per dynamical time step for both schemes, alongside the relative speedup ratio ($t_{\text{2H1FCT}}/t_{\text{TVD-FFSL}}$). The absolute time cost (left Y-axis) reveals a stark contrast between the two methods. The cost of the original 2H1FCT scheme increases linearly and steeply with the addition of new species,

https://doi.org/10.5194/egusphere-2026-2532
Preprint. Discussion started: 22 June 2026

reaching 6.26 seconds per step for 200 species. In contrast, while the TVD-FFSL scheme also exhibits an overall increasing trend, its slope is significantly gentler. For the same 200-species workload, the TVD-FFSL scheme requires only 2.74 seconds. The dashed red line (right Y-axis) shows the speedup ratio of TVD-FFSL relative to 2H1FCT. The TVD-FFSL scheme achieves a remarkable peak speedup of 3.04× when transporting 8 species. As the number of species increases to realistic atmospheric chemistry workloads (e.g., 60 to 200 species), the speedup ratio experiences minor fluctuations but consistently stabilizes at a highly efficient level, generally maintaining a speedup of greater than 2.0×, and concluding at 2.28× for 200 species. Notably, the TVD-FFSL time cost curve displays "plateaus" between 140–160 and 180–200 species, where computational time barely increases despite adding more species. This favorable behavior suggests that the TVD-FFSL algorithm likely benefits from more efficient vectorization, compared to the repetitive operations inherent in the 2H1FCT scheme.

To evaluate the scaling performance at different CPU cores, transport schemes are tested on the U60km mesh with core numbers ranging from 56 to 224. For this test, a constant workload of 120 species is selected. Fig. 13 shows the time cost per dynamical timestep for both schemes (left Y-axis) and the corresponding speedup ratio (right Y-axis). Both the original 2H1FCT scheme and the proposed TVD-FFSL scheme exhibit strong scaling characteristics, with their absolute execution times decreasing monotonically and smoothly as computational resources are added. Crucially, the TVD-FFSL scheme consistently maintains a profound performance advantage across various core counts. For instance, at a baseline of 56 cores, the TVD-FFSL scheme requires only 5.75 seconds per step compared to 14.13 seconds for 2H1FCT. When running on 448 cores, the TVD-FFSL scheme completes in 0.89 seconds, whereas the 2H1FCT scheme still requires nearly 1.89 seconds. The red dashed line in Fig. 13 further quantifies this relative efficiency. The scheme achieves a remarkable peak speedup of 2.46× at 56 cores. As the number of cores increases to 448, the speedup ratio experiences a slight, gradual decline, ultimately stabilizing at 2.12×.

In summary, the efficiency and scalability evaluation unequivocally confirm that the newly developed TVD-FFSL drastically cuts the computational cost of multi-species transport by more than half ($> 2\times$ speedup), without sacrificing algorithmic scalability. It is important to note that the above benchmarks are conducted in a transport-only integration within the parallel framework from iAMAS over only 288 time steps. In the fully coupled Dust21 and Dust25 simulations with 56 species described in the previous section, TVD-FFSL achieves an even higher speedup exceeding 3.75× relative to 2H1FCT (Table 3). This further acceleration likely stems from two factors. Most of the auxiliary arrays introduced by TVD-FFSL are small enough to reside primarily in stack memory, whereas FCT requires frequent allocation/deallocation of heap memory proportional to the number of tracer species. After thousands of integration steps, such repeated heap operations cause memory fragmentation that degrades overall performance. Moreover, TVD-FFSL vectorizes the vertical flux computation along the vertical layer dimension (Algorithm 1), leveraging SIMD-level parallelism for additional speedup. Consequently, while the theoretical reduction in computational cost of TVD-FFSL may be only around 50%, its low memory usage and vectorized implementation yield substantially greater speedup in realistic simulations. Furthermore, the reduced memory allocation frequency and footprint of TVD-FFSL alleviate overall system contention, which also accelerates non-transport modules. As a result, although transport itself is accelerated by 3.75–4.15×, the fraction of transport time only drops from 31–34% to approximately 13% (Table 3).

https://doi.org/10.5194/egusphere-2026-2532
Preprint. Discussion started: 22 June 2026

6 Conclusions

In this study, we developed TVD-FFSL, a computationally efficient tracer transport scheme designed for SCVT-based meshes, and implemented it in the iAMAS model. The scheme combines a TVD horizontal flux operator, an FFSL vertical flux operator, and a second-order TVD Runge-Kutta time integration, ensuring horizontal monotonicity while bypassing vertical CFL restrictions. Furthermore, the vertical PPM reconstruction with monotonicity constraints was vectorized for enhanced performance.

The numerical reliability of TVD-FFSL was rigorously validated. In 2D idealized tests, it demonstrated robust shape-preserving capabilities for discontinuous and strongly deformational flows. Although the restrictive nature of the TVD limiter introduced slightly higher errors and peak clipping compared to the original 2H1FCT scheme, TVD-FFSL exhibited superior convergence rates, rendering the error gap negligible at finer resolutions ($\Delta x \leq 30\ km$). In 3D practical applications, 20-day integrations under frequent dust activity and an extreme dust storm simulation on a 16–60 km variable-resolution grid confirmed its adaptability. The TVD-FFSL scheme maintained long-term numerical stability and achieved simulation accuracy highly comparable to the 2H1FCT scheme under intense synoptic forcing.

The primary motivation behind the design of TVD-FFSL is to achieve high computational efficiency in tracer transport. In standalone transport tests, it provided a stable speedup of over $2.0\times$ across various species counts and CPU cores. Crucially, when fully coupled into iAMAS, this efficiency gain was further amplified due to the scheme's low memory footprint and vectorized vertical implementation. For realistic dust simulations, TVD-FFSL consistently delivered a speedup of $3.75\times$ or greater, significantly reducing the computational overhead of tracer transport without sacrificing physical reliability.

Although both the horizontal TVD and vertical PPM components employ monotonicity limiters individually, the hybrid TVD-FFSL scheme lacks the strict mathematical monotonicity guarantee of FCT-type schemes, especially on unstructured meshes. Nevertheless, no unphysical instabilities or mass accumulations are observed during the extended coupled simulations. Furthermore, the underlying design principles of TVD-FFSL are transferable to other unstructured meshes, offering a pathway toward accelerating high-resolution atmospheric chemistry simulations.

Code and data availability. The code and test cases for the TVD-FFSL scheme are available at https://doi.org/10.5281/zenodo.19486737 (last access: 2026-04-10). The code of the iAMAS model is available upon request by contacting Prof. Zhao (chunzhao@ustc.edu.cn). The ground-based station observations of PM_{10} concentrations are available from the China National Environmental Monitoring Centre (CNEMC) .

https://doi.org/10.5194/egusphere-2026-2532
Preprint. Discussion started: 22 June 2026

Appendix A: Estimation of directional derivatives based on polynomial reconstruction

In Skamarock and Gassmann (2011), the tracer concentration within cell i is represented by a second-order polynomial:

$$\psi = c_0 + c_x x + c_y y + c_{xx} x^2 + c_{xy} xy + c_{yy} y^2 \tag{A1}$$

The coefficients $\mathbf{f} = (c_0, c_x, c_y, c_{xx}, c_{xy}, c_{yy})$ are determined via least squares fitting using cell-centered concentration of cell i and its N first-order neighbors. In SCVTs, N is typically 6, although other values such as 4 and 8 may occur in regions with resolution transition. Following the derivation in Skamarock and Gassmann (2011), the coefficient vector can be expressed as:

$$\mathbf{f} = \mathbf{B}\boldsymbol{\Psi} \tag{A2}$$

where $\mathbf{B}$ is a $(6, N+1)$ matrix that depends solely on the geometric characteristics of SCVTs, and $\boldsymbol{\Psi}$ is an $(N+1) \times 1$ vector containing the values of ψ at cell i and its first-order neighbors. Therefore, the first-order directional derivatives in Eq. 7 can be computed as:

$$\begin{aligned}\left(\frac{\nabla\psi_C \cdot \boldsymbol{d_{CD}}}{|\boldsymbol{d_{CD}}|}\right)_{x=0,y=0} &= \frac{\partial\psi}{\partial x}\cos\theta + \frac{\partial\psi}{\partial y}\sin\theta \\ &= (\cos\theta \mathbf{b_2} + \sin\theta \mathbf{b_3}) \cdot \boldsymbol{\Psi} \\ &= \mathbf{W} \cdot \boldsymbol{\Psi}\end{aligned} \tag{A3}$$

where θ is the azimuth angle of $\boldsymbol{d_{CD}}$ measured from north at cell C, and $\mathbf{b_k}$ denotes the k-th row vector of matrix $\mathbf{B}$. Since the SCVT mesh is static, the weight vector $\mathbf{W}$ can be precomputed from the mesh geometry via the least squares formulation, eliminating repeated matrix inversions during time integration.

Appendix B: Vertical flux based on PPM

The first step of PPM reconstruction is to estimate tracer concentrations at vertical cell interfaces. We employ a fourth-order construction widely used in previous studies (Colella and Woodward, 1984; Skamarock and Gassmann, 2011). For the interface between layers k and $k+1$, the face values are given by:

$$\psi_{k,U} = \psi_{k+1,B} = \frac{7}{12}(\bar{\psi}_{k+1} + \bar{\psi}_k) - \frac{1}{12}(\bar{\psi}_{k+2} + \bar{\psi}_{k-1}) \tag{B1}$$

To maintain monotonicity and prevent overshoot, Colella and Woodward (1984) introduced limiter functions that constrain the parabolic reconstruction when sharp gradients are present. These limiters modify the reconstructed interface values according to these constraints:

$$\psi_{B,k} = \psi_{U,k} = \bar{\psi}_k \qquad \text{if} \quad \left(\psi_{U,k} - \bar{\psi}_k\right)\left(\bar{\psi}_k - \psi_{B,k}\right) \leqslant 0 \tag{B2}$$

$$\psi_{B,k} = 3\bar{\psi}_k - 2\psi_{U,k} \qquad \text{if} \quad (\psi_{U,k} - \psi_{B,k})\left(\bar{\psi}_k - \frac{1}{2}(\psi_{B,k} + \psi_{U,k})\right) > \frac{(\psi_{U,k} - \psi_{B,k})^2}{6} \tag{B3}$$

$$\psi_{U,k} = 3\bar{\psi}_k - 2\psi_{B,k} \qquad \text{if} \quad -\frac{(\psi_{U,k} - \psi_{B,k})^2}{6} > (\psi_{U,k} - \psi_{B,k})\left(\bar{\psi}_k - \frac{1}{2}(\psi_{B,k} + \psi_{U,k})\right) \tag{B4}$$

https://doi.org/10.5194/egusphere-2026-2532
Preprint. Discussion started: 22 June 2026

Based on these interface values, a parabolic function (Colella and Woodward, 1984) representing the tracer concentration distribution within layer k can be constructed as follows:

$$\psi(\xi) = \psi_{B,k} + \xi\left[\Delta\psi_k + \psi_{6,k}(1-\xi)\right] \tag{B5}$$

where, $\xi \in [0,1]$ is the fraction of the thickness of layer k, $\Delta\psi_k = \psi_{U,k} - \psi_{B,k}$, and $\psi_{6,k} = 6\left[\bar{\psi}_k - \frac{1}{2}\left(\psi_{B,k} + \psi_{U,k}\right)\right]$. The above construction ensures mass conservation, expressed as $\int_0^1 \psi(\xi)d\xi\Delta z_k = \bar{\psi}_k\Delta z_k$.

Consequently, the vertical flux with upward velocity at the interface is given by:

$$F_k^v = \sum_{k_s}^{k_e} \rho_k\bar{\psi}_k\Delta z_k + \rho\Delta z \int_{1-\xi}^{1} \psi(\xi)d\xi \tag{B6}$$

where k_s and k_e denote the starting and ending indices of complete grid cells traversed by the backward trajectory. For the vast majority of grid cells where CFL < 1, the summation term vanishes, and only the integral term contributes to the flux. For downward wind conditions, the integration limits become 0 and ξ. The integral term can be transformed as:

$$\int_{\xi_s}^{\xi_e} \psi(\xi)d\xi = \psi_{B,k}\xi\Big|_{\xi_s}^{\xi_e} + (\Delta\psi_k + \psi_{6,k})\xi^2\Big|_{\xi_s}^{\xi_e} - \psi_{6,k}\xi^3\Big|_{\xi_s}^{\xi_e} \tag{B7}$$

The ξ-dependent terms are computed once for all tracers, exploiting a key efficiency advantage of the FFSL scheme: the trajectory (and thus ξ) depends only on wind direction, whereas coefficients in Eq. B7 must be computed separately for each species due to their dependence on tracer concentration.

Appendix C: Error norms

The L_2 error norm is defined as:

$$L_2 = \frac{\sum_i A_i\left(\bar{\psi}_i - \psi_{t,i}\right)^2}{\sum_i A_i\psi_{t,i}^2} \tag{C1}$$

where i is the cell index, A_i is the area of cell i, $\bar{\psi}_i$ is the numerical solution, and $\psi_{t,i}$ is the true solution.

The L_{inf} error norm is computed as:

$$L_{\text{inf}} = \frac{\max_i|\bar{\psi}_i - \psi_{t,i}|}{\max_i|\psi_{t,i}|} \tag{C2}$$

Author contributions. Gudongze Li developed the TVD-FFSL scheme and prepared the manuscript. Chun Zhao supervised the study and reviewed the results. Yinhua Xia and Li Dong provided valuable guidance on the scheme development and results analysis. Yibo Xue and Xiao-Xiao Zhang contributed to the design and analysis of the dust storm experiments. Jun Gu, Jiawang Feng and Zihan Xia developed the iAMAS model that served as the foundation for this study. All authors contributed to the writing and revision of the manuscript.

https://doi.org/10.5194/egusphere-2026-2532
Preprint. Discussion started: 22 June 2026

Competing interests. The authors declare that they have no conflict of interest.

Acknowledgements. This work was supported by the Young Students' Basic Research Project (Doctoral Candidates) of the National Natural Science Foundation of China (Grant No. 424B2042), Shanghai Institute for Mathematics and Interdisciplinary Sciences grant (Grant No. SIMIS-ID-2024-XD), Jing-Jin-Ji Regional Integrated Environmental Improvement-National Science and Technology Major Project (Grant No. 2025ZD1201700), the Strategic Priority Research Program of the Chinese Academy of Sciences (Grant No. XDB0500303), and the Cultivation Plan for Tianshan Talent Scholar (Grant No. 2022TSYCCX0012). The study used the computing resources from the Supercomputing Center of the University of Science and Technology of China (USTC) and the Qingdao Supercomputing and Big Data Center.

https://doi.org/10.5194/egusphere-2026-2532
Preprint. Discussion started: 22 June 2026

References

Blossey, P. N. and Durran, D. R.: Selective monotonicity preservation in scalar advection, Journal of Computational Physics, 227, 5160–5183, https://doi.org/10.1016/j.jcp.2008.01.043, 2008.

Bosler, P. A., Kent, J., Krasny, R., and Jablonowski, C.: A Lagrangian particle method with remeshing for tracer transport on the sphere, Journal of Computational Physics, 340, 639–654, https://doi.org/10.1016/j.jcp.2017.03.052, 2017.

Bruner, C., Walters, R., Bruner, C., and Walters, R.: Parallelization of the Euler equations on unstructured grids, in: 13th Computational Fluid Dynamics Conference, American Institute of Aeronautics and Astronautics, https://doi.org/10.2514/6.1997-1894, 1997.

Chen, F., Zhang, W., Mfarrej, M. F. B., Saleem, M. H., Khan, K. A., Ma, J., Raposo, A., and Han, H.: Breathing in danger: Understanding the multifaceted impact of air pollution on health impacts, Ecotoxicology and Environmental Safety, 280, 116 532, https://doi.org/10.1016/j.ecoenv.2024.116532, 2024.

Chopp, D. L.: Flow Control, in: Introduction to High Performance Scientific Computing, pp. 51–58, Society for Industrial and Applied Mathematics, https://doi.org/10.1137/1.9781611975642.ch5, 2019.

Coen, J. L., Cameron, M., Michalakes, J., Patton, E. G., Riggan, P. J., and Yedinak, K. M.: WRF-Fire: Coupled Weather–Wildland Fire Modeling with the Weather Research and Forecasting Model, Journal of Applied Meteorology and Climatology, 52, 16–38, https://doi.org/10.1175/jamc-d-12-023.1, 2013.

Colella, P. and Woodward, P. R.: The Piecewise Parabolic Method (PPM) for gas-dynamical simulations, Journal of Computational Physics, 54, 174–201, https://doi.org/10.1016/0021-9991(84)90143-8, 1984.

Darwish, M. and Moukalled, F.: TVD schemes for unstructured grids, International Journal of Heat and Mass Transfer, 46, 599–611, https://doi.org/10.1016/s0017-9310(02)00330-7, 2003.

Dong, L., Wang, B., and Liu, L.: A Lagrangian advection scheme with shape matrix (LASM) for solving advection problems, Geoscientific Model Development, 7, 2951–2968, https://doi.org/10.5194/gmd-7-2951-2014, 2014.

Dubey, S., Mittal, R., and Lauritzen, P. H.: A flux-form conservative semi-Lagrangian multitracer transport scheme (FF-CSLAM) for icosahedral-hexagonal grids, Journal of Advances in Modeling Earth Systems, 6, 332–356, https://doi.org/10.1002/2013ms000259, 2014.

Dukowicz, J. K. and Kodis, J. W.: Accurate Conservative Remapping (Rezoning) for Arbitrary Lagrangian-Eulerian Computations, SIAM Journal on Scientific and Statistical Computing, 8, 305–321, https://doi.org/10.1137/0908037, 1987.

Engwirda, D.: JIGSAW-GEO (1.0): locally orthogonal staggered unstructured grid generation for general circulation modelling on the sphere, Geoscientific Model Development, 10, 2117–2140, https://doi.org/10.5194/gmd-10-2117-2017, 2017.

Feng, J., Zhao, C., Du, Q., Xu, M., Gu, J., Hu, Z., and Chen, Y.: Simulating Atmospheric Dust With a Global Variable-Resolution Model: Model Description and Impacts of Mesh Refinement, Journal of Advances in Modeling Earth Systems, 15, https://doi.org/10.1029/2023ms003636, 2023.

Feng, J., Zhao, C., Gu, J., Li, G., Xu, M., Lin, S., and Feng, J.: Dust impacts on the Indian summer monsoon: chaotic or physical effect?, Atmospheric Chemistry and Physics, 25, 12 051–12 068, https://doi.org/10.5194/acp-25-12051-2025, 2025.

Giraldo, F. X.: Trajectory Calculations for Spherical Geodesic Grids in Cartesian Space, Monthly Weather Review, 127, 1651–1662, https://doi.org/10.1175/1520-0493(1999)127<1651:tcfsgg>2.0.co;2, 1999.

Gottlieb, S. and Shu, C.-W.: Total variation diminishing Runge-Kutta schemes, Mathematics of Computation, 67, 73–85, https://doi.org/10.1090/s0025-5718-98-00913-2, 1998.

https://doi.org/10.5194/egusphere-2026-2532
Preprint. Discussion started: 22 June 2026

Gu, J., Feng, J., Hao, X., Fang, T., Zhao, C., An, H., Chen, J., Xu, M., Li, J., Han, W., Yang, C., Li, F., and Chen, D.: Establishing a non-hydrostatic global atmospheric modeling system at 3-km horizontal resolution with aerosol feedbacks on the Sunway supercomputer of China, Science Bulletin, 67, 1170–1181, https://doi.org/10.1016/j.scib.2022.03.009, 2022.

Gu, J., Zhao, C., Xu, M., Feng, J., Li, G., Zhao, Y., Hao, X., Chen, J., and An, H.: Global convection-permitting model improves subseasonal forecast of plum rain around Japan, Environmental Research Letters, 19, 104 021, https://doi.org/10.1088/1748-9326/ad71e2, 2024.

Gu, J., Zhao, C., Li, G., Feng, J., Xu, M., Du, Q., Xia, Z., Li, Y., Chen, G., Hao, X., Chen, J., and An, H.: Pronounced advance on typhoon track forecast with global convection-permitting model, Science Bulletin, 70, 1424–1428, https://doi.org/10.1016/j.scib.2025.01.032, 2025.

Harris, L. M., Lauritzen, P. H., and Mittal, R.: A flux-form version of the conservative semi-Lagrangian multi-tracer transport scheme (CSLAM) on the cubed sphere grid, Journal of Computational Physics, 230, 1215–1237, https://doi.org/10.1016/j.jcp.2010.11.001, 2011.

Hirt, C., Amsden, A., and Cook, J.: An arbitrary Lagrangian-Eulerian computing method for all flow speeds, Journal of Computational Physics, 14, 227–253, https://doi.org/10.1016/0021-9991(74)90051-5, 1974.

Hoppe, C. M., Hoffmann, L., Konopka, P., Grooß, J.-U., Ploeger, F., Günther, G., Jöckel, P., and Müller, R.: The implementation of the CLaMS Lagrangian transport core into the chemistry climate model EMAC 2.40.1: application on age of air and transport of long-lived trace species, Geoscientific Model Development, 7, 2639–2651, https://doi.org/10.5194/gmd-7-2639-2014, 2014.

Hou, J., Simons, F., and Hinkelmann, R.: Improved total variation diminishing schemes for advection simulation on arbitrary grids, International Journal for Numerical Methods in Fluids, 70, 359–382, https://doi.org/10.1002/fld.2700, 2011.

Hou, J., Simons, F., and Hinkelmann, R.: A new TVD method for advection simulation on 2D unstructured grids, International Journal for Numerical Methods in Fluids, 71, 1260–1281, https://doi.org/10.1002/fld.3709, 2012.

Iske, A. and Käser, M.: Conservative semi-Lagrangian advection on adaptive unstructured meshes, Numerical Methods for Partial Differential Equations, 20, 388–411, https://doi.org/https://doi.org/10.1002/num.10100, 2004.

Klemp, J. B.: A Terrain-Following Coordinate with Smoothed Coordinate Surfaces, Monthly Weather Review, 139, 2163–2169, https://doi.org/10.1175/mwr-d-10-05046.1, 2011.

Klemp, J. B., Skamarock, W. C., and Dudhia, J.: Conservative Split-Explicit Time Integration Methods for the Compressible Nonhydrostatic Equations, Monthly Weather Review, 135, 2897–2913, https://doi.org/10.1175/mwr3440.1, 2007.

Koren, B.: A robust upwind discretization method for advection, diffusion and source terms, pp. 117–138, Notes on Numerical Fluid Mechanics, Vieweg, Germany, 1993.

Lauritzen, P. H., Nair, R. D., and Ullrich, P. A.: A conservative semi-Lagrangian multi-tracer transport scheme (CSLAM) on the cubed-sphere grid, Journal of Computational Physics, 229, 1401–1424, https://doi.org/10.1016/j.jcp.2009.10.036, 2010.

Lauritzen, P. H., Erath, C., and Mittal, R.: On simplifying 'incremental remap'–based transport schemes, Journal of Computational Physics, https://doi.org/10.1016/j.jcp.2011.06.030, 2011.

Li, G., Zhao, C., Gu, J., Feng, J., Xu, M., Hao, X., Chen, J., An, H., Cai, W., and Geng, T.: Excessive equatorial light rain causes modeling dry bias of Indian summer monsoon rainfall, npj Climate and Atmospheric Science, 8, https://doi.org/10.1038/s41612-025-00916-1, 2025.

Li, L.-x., Liao, H.-s., and Qi, L.-j.: An improved r-factor algorithm for TVD schemes, International Journal of Heat and Mass Transfer, 51, 610–617, https://doi.org/10.1016/j.ijheatmasstransfer.2007.04.051, 2008.

Li, Q., Sheng, B., Huang, J., Li, C., Song, Z., Chao, L., Sun, W., Yang, Y., Jiao, B., Guo, Z., Liao, L., Li, X., Sun, C., Li, W., Huang, B., Dong, W., and Jones, P.: Different climate response persistence causes warming trend unevenness at continental scales, Nature Climate Change, 12, 343–349, https://doi.org/10.1038/s41558-022-01313-9, 2022.

https://doi.org/10.5194/egusphere-2026-2532
Preprint. Discussion started: 22 June 2026

Lin, S.-J. and Rood, R. B.: Multidimensional Flux-Form Semi-Lagrangian Transport Schemes, Monthly Weather Review, 124, 2046–2070, https://doi.org/10.1175/1520-0493(1996)124<2046:mffslt>2.0.co;2, 1996.

Lipscomb, W. H. and Ringler, T. D.: An Incremental Remapping Transport Scheme on a Spherical Geodesic Grid, Monthly Weather Review, 133, 2335–2350, https://doi.org/10.1175/mwr2983.1, 2005.

McKenna, D. S., Konopka, P., Grooß, J., Günther, G., Müller, R., Spang, R., Offermann, D., and Orsolini, Y.: A new Chemical Lagrangian Model of the Stratosphere (CLaMS) 1. Formulation of advection and mixing, Journal of Geophysical Research: Atmospheres, 107, https://doi.org/10.1029/2000jd000114, 2002.

Reithmeier, C. and Sausen, R.: ATTILA: atmospheric tracer transport in a Lagrangian model, Tellus B, 54, 278–299, https://doi.org/10.1034/j.1600-0889.2002.01236.x, 2002.

Renka, R. J.: Algorithm 772: STRIPACK: Delaunay triangulation and Voronoi diagram on the surface of a sphere, ACM Transactions on Mathematical Software, 23, 416–434, https://doi.org/10.1145/275323.275329, 1997.

Richard, G., Sawyer, W. E., and Sharipov, A.: Environmental Impacts of Air Pollution, pp. 47–76, Springer Nature Switzerland, Cham, https://doi.org/10.1007/698_2024_1114, 2024.

Rosatti, G., Cesari, D., and Bonaventura, L.: Semi-implicit, semi-Lagrangian modelling for environmental problems on staggered Cartesian grids with cut cells, Journal of Computational Physics, 204, 353–377, https://doi.org/10.1016/j.jcp.2004.10.013, 2005.

Shu, C.-W. and Osher, S.: Efficient implementation of essentially non-oscillatory shock-capturing schemes, Journal of Computational Physics, 77, 439–471, https://doi.org/10.1016/0021-9991(88)90177-5, 1988.

Simpson, I. R., Rosenbloom, N., Danabasoglu, G., Deser, C., Yeager, S. G., McCluskey, C. S., Yamaguchi, R., Lamarque, J.-F., Tilmes, S., Mills, M. J., and Rodgers, K. B.: The CESM2 Single-Forcing Large Ensemble and Comparison to CESM1: Implications for Experimental Design, Journal of Climate, 36, 5687–5711, https://doi.org/10.1175/jcli-d-22-0666.1, 2023.

Skamarock, W. C.: Positive-Definite and Monotonic Limiters for Unrestricted-Time-Step Transport Schemes, Monthly Weather Review, 134, 2241–2250, https://doi.org/10.1175/mwr3170.1, 2006.

Skamarock, W. C. and Gassmann, A.: Conservative Transport Schemes for Spherical Geodesic Grids: High-Order Flux Operators for ODE-Based Time Integration, Monthly Weather Review, 139, 2962–2975, https://doi.org/10.1175/mwr-d-10-05056.1, 2011.

Skamarock, W. C. and Menchaca, M.: Conservative Transport Schemes for Spherical Geodesic Grids: High-Order Reconstructions for Forward-in-Time Schemes, Monthly Weather Review, 138, 4497–4508, https://doi.org/10.1175/2010mwr3390.1, 2010.

Skamarock, W. C., Klemp, J. B., Duda, M. G., Fowler, L. D., Park, S.-H., and Ringler, T. D.: A Multiscale Nonhydrostatic Atmospheric Model Using Centroidal Voronoi Tesselations and C-Grid Staggering, Monthly Weather Review, 140, 3090–3105, https://doi.org/10.1175/mwr-d-11-00215.1, 2012.

Skamarock, W. C., Klemp, J. B., Dudhia, J., Gill, D. O., Liu, Z., Berner, J., Wang, W., Powers, J. G., Duda, M. G., Barker, D. M., and Huang, X.-Y.: A Description of the Advanced Research WRF Model Version 4, Tech. rep., NSF National Center for Atmospheric Research, https://doi.org/10.5065/1DFH-6P97, 2019.

Stenke, A. and Grewe, V.: Simulation of stratospheric water vapor trends: Impact on stratospheric ozone chemistry, Atmospheric Chemistry and Physics, 5, 1257–1272, https://doi.org/10.5194/acp-5-1257-2005, 2005.

Stohl, A., Forster, C., Frank, A., Seibert, P., and Wotawa, G.: Technical note: The Lagrangian particle dispersion model FLEXPART version 6.2, Atmospheric Chemistry and Physics, 5, 2461–2474, https://doi.org/10.5194/acp-5-2461-2005, 2005.

Sweby, P. K.: High Resolution Schemes Using Flux Limiters for Hyperbolic Conservation Laws, SIAM Journal on Numerical Analysis, 21, 995–1011, https://doi.org/10.1137/0721062, 1984.

https://doi.org/10.5194/egusphere-2026-2532
Preprint. Discussion started: 22 June 2026

Tang, S.: Adaptive symmetric flux limiters with long computation times for hyperbolic conservation laws, Results in Applied Mathematics, 20, 100 410, https://doi.org/10.1016/j.rinam.2023.100410, 2023.

Ullrich, P. A., Lauritzen, P. H., and Jablonowski, C.: Some considerations for high-order 'incremental remap'-based transport schemes: edges, reconstructions, and area integration, International Journal for Numerical Methods in Fluids, 71, 1131–1151, https://doi.org/10.1002/fld.3703, 2012.

Wang, H., Skamarock, W. C., and Feingold, G.: Evaluation of Scalar Advection Schemes in the Advanced Research WRF Model Using Large-Eddy Simulations of Aerosol–Cloud Interactions, Monthly Weather Review, 137, 2547–2558, https://doi.org/10.1175/2009mwr2820.1, 2009.

Wicker, L. J. and Skamarock, W. C.: Time-Splitting Methods for Elastic Models Using Forward Time Schemes, Monthly Weather Review, 130, 2088–2097, https://doi.org/10.1175/1520-0493(2002)130<2088:tsmfem>2.0.co;2, 2002.

Williamson, D. L., Drake, J. B., Hack, J. J., Jakob, R., and Swarztrauber, P. N.: A standard test set for numerical approximations to the shallow water equations in spherical geometry, Journal of Computational Physics, 102, 211–224, https://doi.org/10.1016/s0021-9991(05)80016-6, 1992.

Yang, Q., Zhao, C., Feng, J., Li, G., Gu, J., Xia, Z., Xu, M., and Yang, Z.: Comprehensive evaluation of iAMAS (v1.0) in simulating Antarctic meteorological fields with observations and reanalysis, Geoscientific Model Development, 18, 5373–5396, https://doi.org/10.5194/gmd-18-5373-2025, 2025.

Yoon, J. W., Lee, E., and Park, S. K.: Improving the Asian dust storm prediction using WRF-Chem through combinational optimization of physical parameterization schemes, Atmospheric Environment, 326, 120 461, https://doi.org/10.1016/j.atmosenv.2024.120461, 2024.

Zalesak, S. T.: Fully multidimensional flux-corrected transport algorithms for fluids, Journal of Computational Physics, 31, 335–362, https://doi.org/10.1016/0021-9991(79)90051-2, 1979.

https://doi.org/10.5194/egusphere-2026-2532
Preprint. Discussion started: 22 June 2026

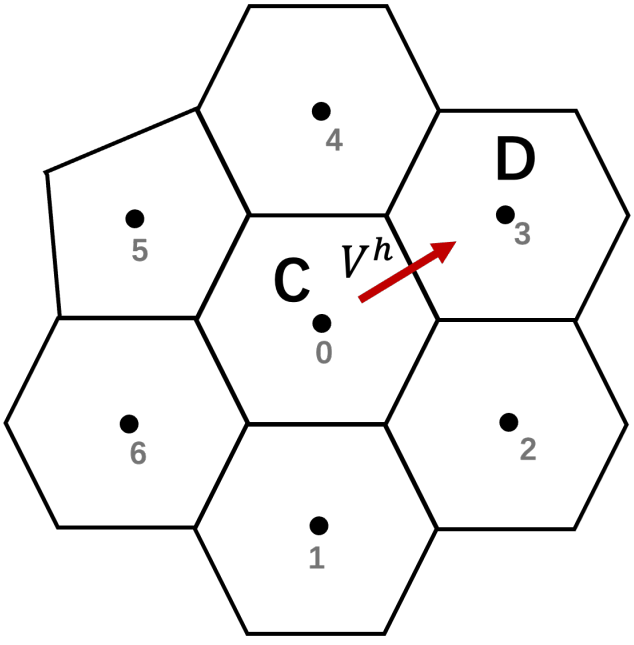

Figure 1. Illustration of SCVT with C-grid staggering. Black dots denote cell centers, while red arrows represent velocity normal to cell faces. In the notation used, cell C refers to the upstream cell (0) and cell D refers to the downstream cell (3) when velocity flows from cell 0 to cell 3.

https://doi.org/10.5194/egusphere-2026-2532
Preprint. Discussion started: 22 June 2026

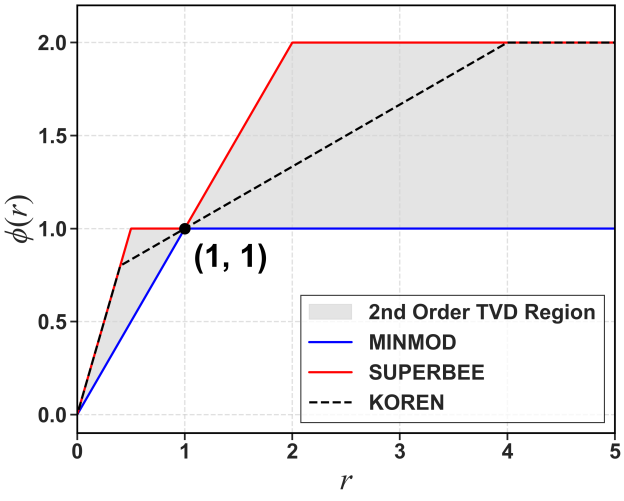

Figure 2. Second-order total variation diminishing (TVD) region and KOREN limiter function.

https://doi.org/10.5194/egusphere-2026-2532
Preprint. Discussion started: 22 June 2026

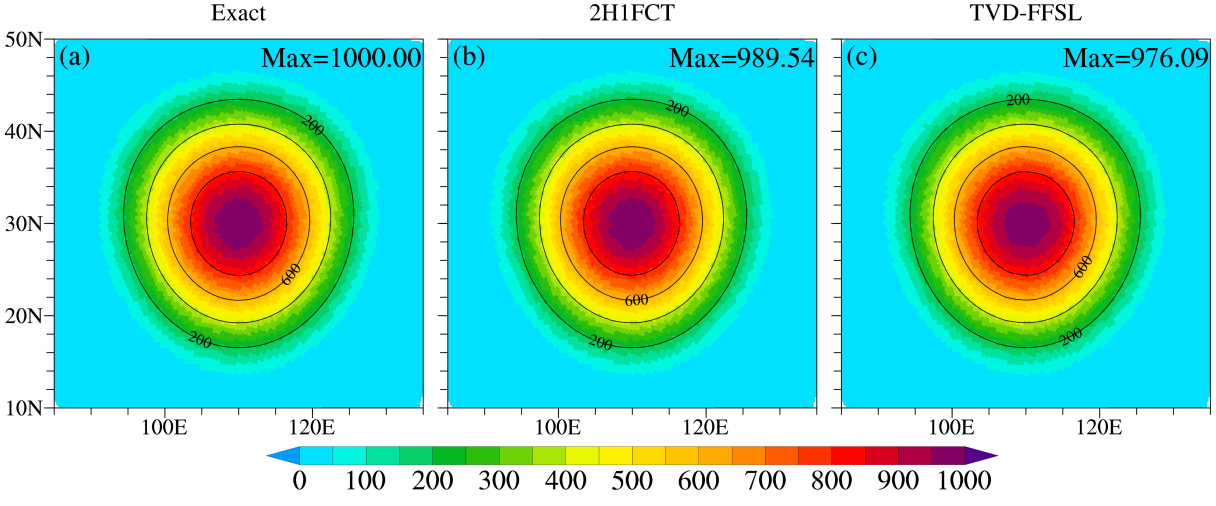

Figure 3. Cosine bell under the solid body rotation test on the U60km mesh at $t = T$. (**a**) Exact solution. (**b**) Result of the original 2H1FCT scheme in iAMAS. (**c**) Result of the TVD-FFSL hybrid scheme.

https://doi.org/10.5194/egusphere-2026-2532
Preprint. Discussion started: 22 June 2026

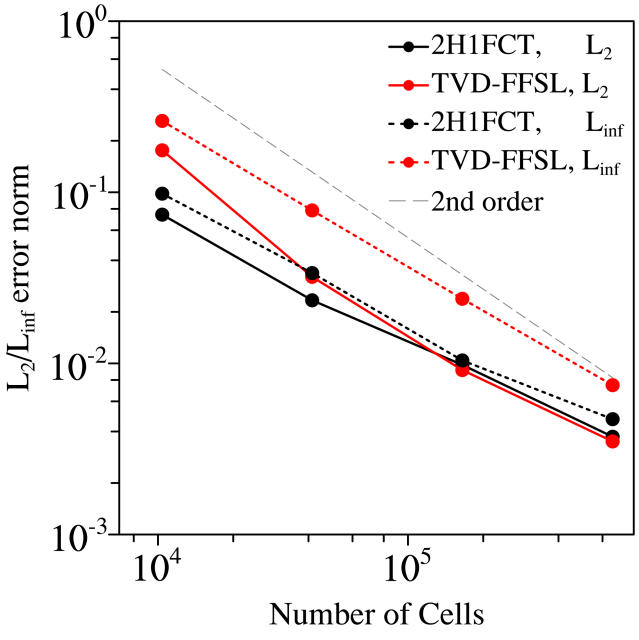

Figure 4. The L_2 and L_{inf} error norms of the cosine bell under the solid body rotation test.

https://doi.org/10.5194/egusphere-2026-2532
Preprint. Discussion started: 22 June 2026

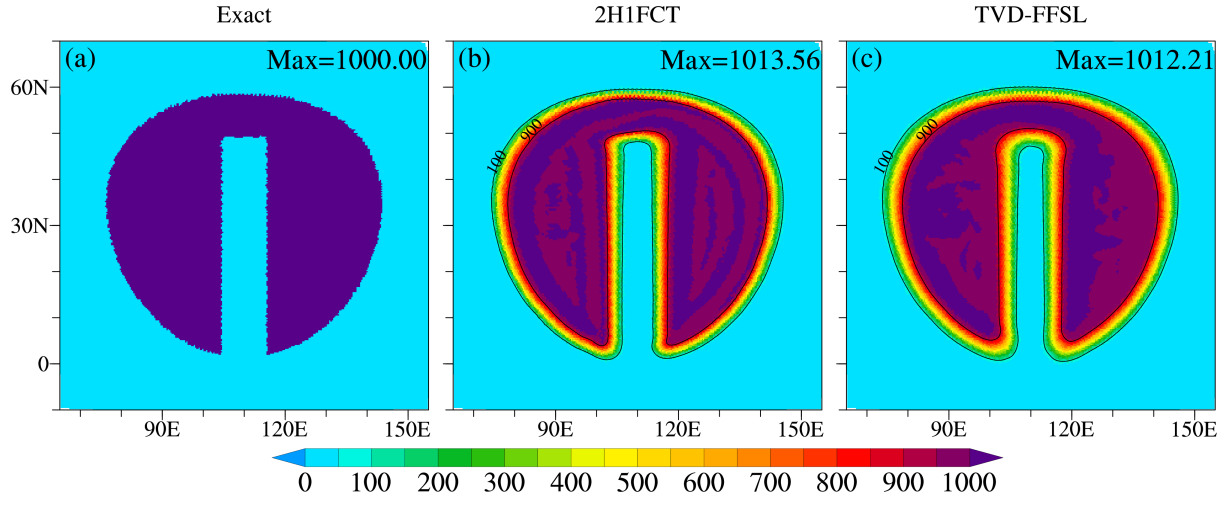

Figure 5. Slotted cylinder under the solid body rotation test on the U60km mesh at $t = T$. (**a**) Exact solution. (**b**) Result of the original 2H1FCT scheme in iAMAS. (**c**) Result of the TVD-FFSL hybrid scheme.

https://doi.org/10.5194/egusphere-2026-2532
Preprint. Discussion started: 22 June 2026

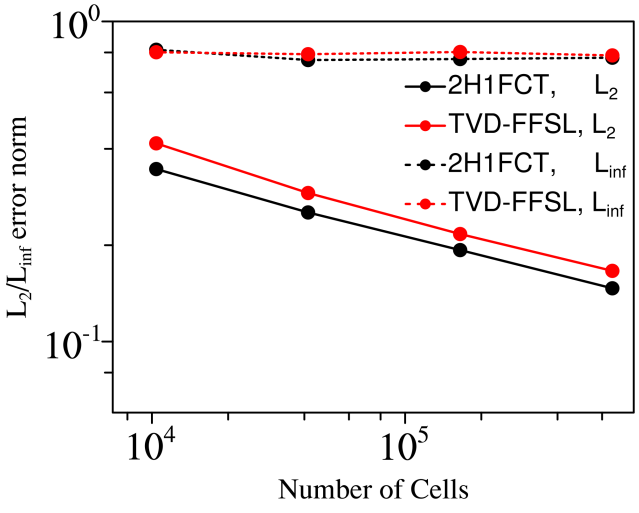

Figure 6. The L_2 and L_{inf} error norms of the slotted cylinder under the solid body rotation test.

https://doi.org/10.5194/egusphere-2026-2532
Preprint. Discussion started: 22 June 2026

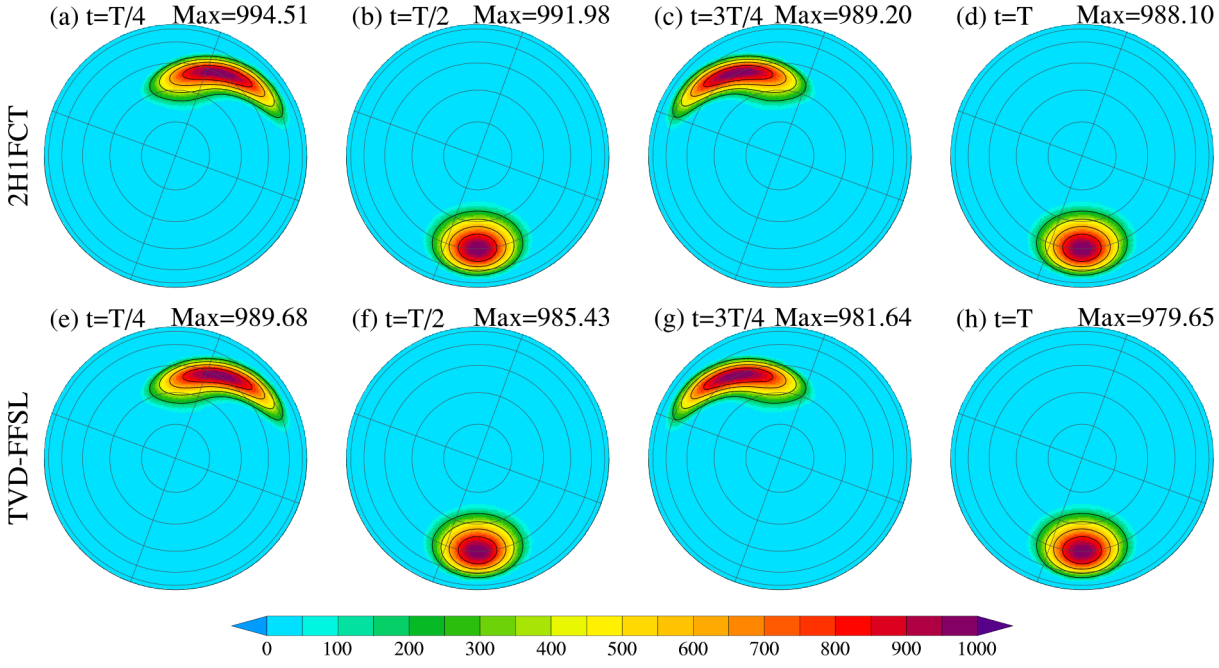

Figure 7. Cosine bell under deformational flow on the U60km mesh. (a-d) Results of 2H1FCT at $t = \frac{T}{4}, \frac{T}{2}, \frac{3T}{4}, T$. (e-h) Results of TVD-FFSL at $t = \frac{T}{4}, \frac{T}{2}, \frac{3T}{4}, T$.

https://doi.org/10.5194/egusphere-2026-2532
Preprint. Discussion started: 22 June 2026

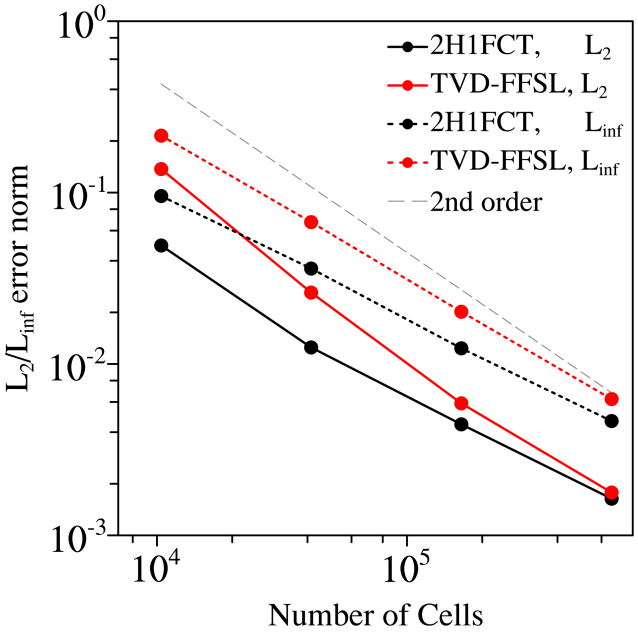

Figure 8. The L_2 and L_{inf} error norms of the cosine bell under deformational flow.

https://doi.org/10.5194/egusphere-2026-2532
Preprint. Discussion started: 22 June 2026

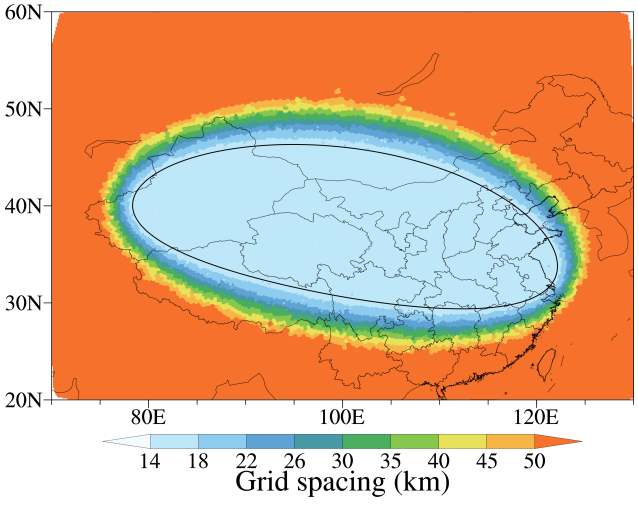

Figure 9. Grid spacing distribution of the V16km mesh. The black solid line surrounds the region with resolution of 16 km.

https://doi.org/10.5194/egusphere-2026-2532
Preprint. Discussion started: 22 June 2026

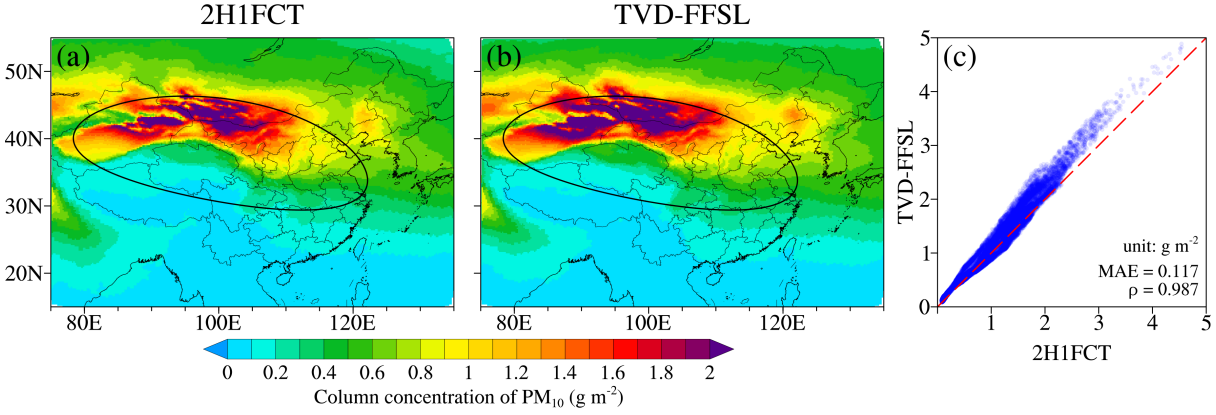

Figure 10. The column concentration of PM_{10} averged over the period of 12–31 March, 2021, simulated by iAMAS configured with (**a**) 2H1FCT and (**b**) TVD-FFSL schemes. The black solid line surrounds the region with resolution of 16 km. (**c**) The scatter plot of averaged PM_{10} column concentration within the refined region.

https://doi.org/10.5194/egusphere-2026-2532
Preprint. Discussion started: 22 June 2026

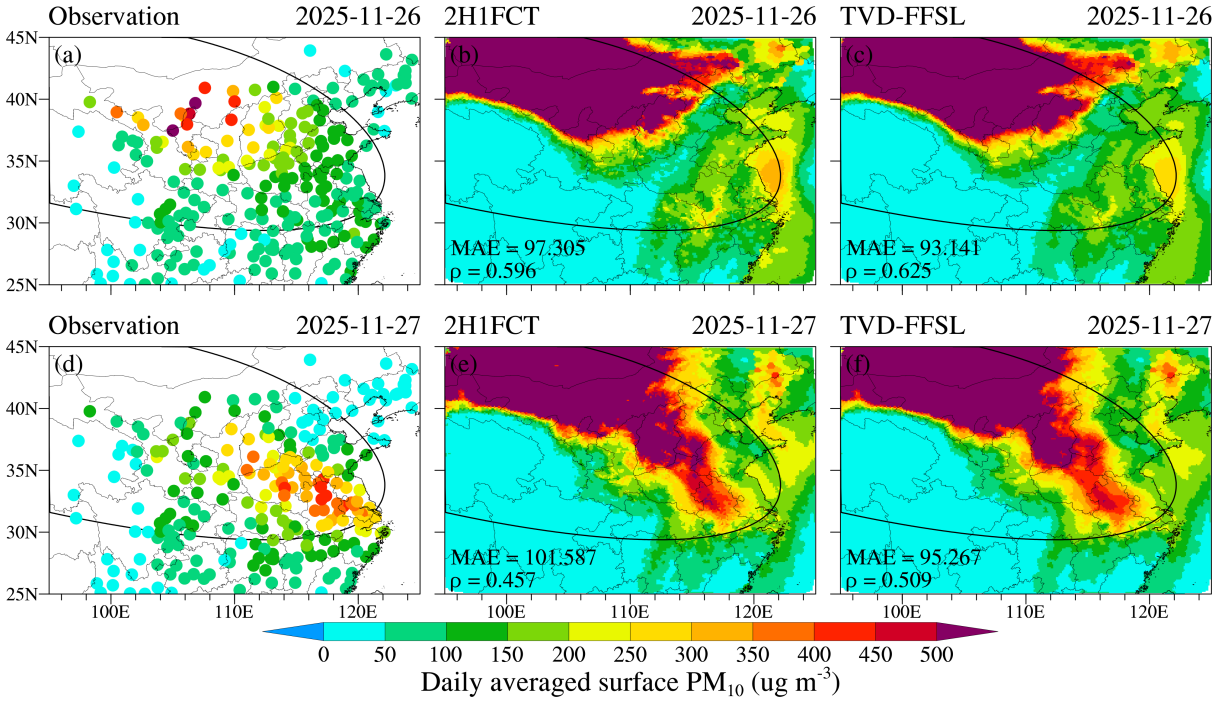

Figure 11. The daily averged surface PM_{10} at Nov 26, 2025, in (**a**) observation, simulations with (**b**) 2H1FCT and (**c**) TVD-FFSL schemes. The black solid line surrounds the region with resolution of 16 km. (**d-f**) the daily averged surface PM_{10} at Nov 27, 2025. The MAE and ρ are computed between simulated and observed values at each station.

https://doi.org/10.5194/egusphere-2026-2532
Preprint. Discussion started: 22 June 2026

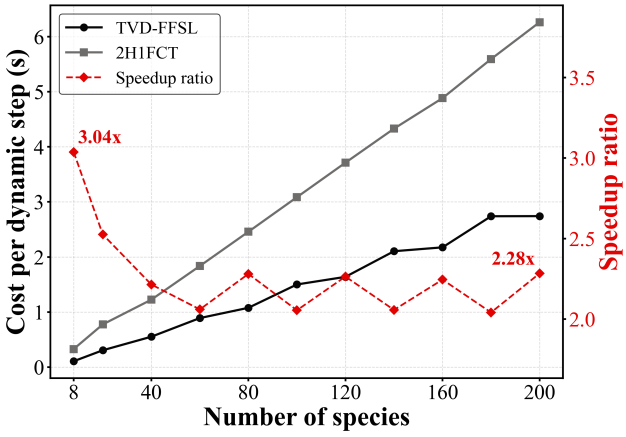

Figure 12. Time cost per dynamical timestep for 2H1FCT and TVD-FFSL (left Y-axis) and the speedup ratio ($t_{\text{2H1FCT}}/t_{\text{TVD-FFSL}}$, right Y-axis) on U60km using 8x28 cores (Intel Xeon E5-2680 v4, 2.40 GHz) with varying tracer species.

https://doi.org/10.5194/egusphere-2026-2532
Preprint. Discussion started: 22 June 2026

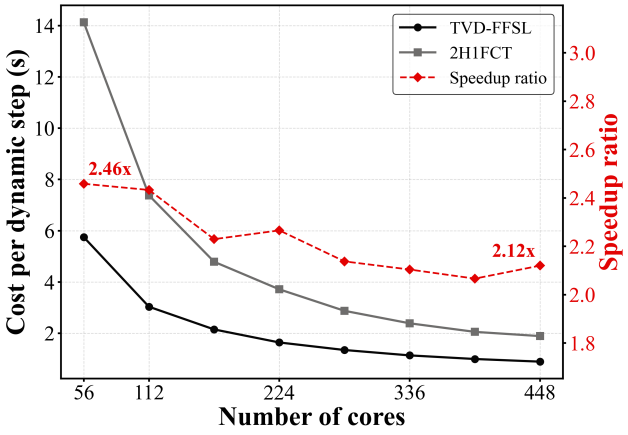

Figure 13. Time cost per dynamical timestep for 2H1FCT and TVD-FFSL (left Y-axis) and the speedup ratio ($t_{\text{2H1FCT}}/t_{\text{TVD-FFSL}}$, right Y-axis) on U60km with 120 species using different cores.

https://doi.org/10.5194/egusphere-2026-2532
Preprint. Discussion started: 22 June 2026

Table 1. Mesh configurations used in the numerical experiments.

Mesh name	Resolution	Cells
U240km	240 km	10,398
U120km	120 km	41,375
U60km	60 km	164,971
U30km	30 km	658,591
V16km	16–60 km	193,543

https://doi.org/10.5194/egusphere-2026-2532
Preprint. Discussion started: 22 June 2026

Table 2. Convergence rates of the cosine bell test under solid body rotation and deformational flow.

Resolution	Solid body rotation		Deformational flow	
	2H1FCT	TVD-FFSL	2H1FCT	TVD-FFSL
240km–120km	1.663	2.457	1.976	2.394
120km–60km	1.254	1.809	1.490	2.147
60km–30km	1.395	1.386	1.441	1.728

https://doi.org/10.5194/egusphere-2026-2532
Preprint. Discussion started: 22 June 2026

Table 3. Comparison of total wall-clock time cost for tracer transport between the 2H1FCT and TVD-FFSL schemes in two dust storm simulations with V16km mesh: Dust21 (20 days, 512 cores) and Dust25 (6 days, 256 cores).

Dust episode	Dust21		Dust25	
	2H1FCT	TVD-FFSL	2H1FCT	TVD-FFSL
Transport fraction (%)	31.48	13.06	34.33	12.94
Transport time (s)	32659.1	8712.2	20869.1	5034.0
Speedup		**3.75**×		**4.15**×

https://doi.org/10.5194/egusphere-2026-2532
Preprint. Discussion started: 22 June 2026

Algorithm 1 Vectorized branch-free PPM reconstruction

Input: Cell average array $\bar{\psi}$, interface arrays $\boldsymbol{\psi}_B$, $\boldsymbol{\psi}_U$, for all vertical layers $k \in [0, N]$
Output: Polynomial coefficients $\boldsymbol{C}_0$, $\boldsymbol{C}_1$, $\boldsymbol{C}_2$
Step 1: Compute initial gradients and curvatures
  $\Delta\boldsymbol{\psi} \leftarrow \boldsymbol{\psi}_U - \boldsymbol{\psi}_B$
  $\boldsymbol{\psi}_6 \leftarrow 6\bar{\boldsymbol{\psi}} - 3(\boldsymbol{\psi}_B + \boldsymbol{\psi}_U)$
Step 2: Evaluate limiter conditions as boolean masks
  $\boldsymbol{M}_1 \leftarrow (\boldsymbol{\psi}_U - \bar{\boldsymbol{\psi}}) \circ (\bar{\boldsymbol{\psi}} - \boldsymbol{\psi}_B) \leq 0$
  $\boldsymbol{M}_2 \leftarrow \neg\boldsymbol{M}_1 \wedge (\Delta\boldsymbol{\psi} \circ \boldsymbol{\psi}_6 > \Delta\boldsymbol{\psi}^2)$
  $\boldsymbol{M}_3 \leftarrow \neg\boldsymbol{M}_1 \wedge (\Delta\boldsymbol{\psi} \circ \boldsymbol{\psi}_6 < -\Delta\boldsymbol{\psi}^2)$
Step 3: Update interfaces using masked operations
! Note: MERGE$(T, F, Mask)$ returns T where $Mask$ is true, else F
  $\boldsymbol{\psi}_B \leftarrow$ MERGE$(3\bar{\boldsymbol{\psi}} - 2\boldsymbol{\psi}_U, \boldsymbol{\psi}_B, \boldsymbol{M}_2)$
  $\boldsymbol{\psi}_B \leftarrow$ MERGE$(\bar{\boldsymbol{\psi}}, \boldsymbol{\psi}_B, \boldsymbol{M}_1)$
  $\boldsymbol{\psi}_U \leftarrow$ MERGE$(3\bar{\boldsymbol{\psi}} - 2\boldsymbol{\psi}_B, \boldsymbol{\psi}_U, \boldsymbol{M}_3)$
  $\boldsymbol{\psi}_U \leftarrow$ MERGE$(\bar{\boldsymbol{\psi}}, \boldsymbol{\psi}_U, \boldsymbol{M}_1)$
Step 4: Compute final polynomial coefficients
  $\Delta\boldsymbol{\psi} \leftarrow \boldsymbol{\psi}_U - \boldsymbol{\psi}_B$
  $\boldsymbol{\psi}_6 \leftarrow 6\bar{\boldsymbol{\psi}} - 3(\boldsymbol{\psi}_B + \boldsymbol{\psi}_U)$
  $\boldsymbol{C}_0 \leftarrow \boldsymbol{\psi}_B$
  $\boldsymbol{C}_1 \leftarrow \Delta\boldsymbol{\psi} + \boldsymbol{\psi}_6$
  $\boldsymbol{C}_2 \leftarrow -\boldsymbol{\psi}_6$